On-Orbit Characterization of the VIIRS Solar Diffuser and Attenuation Screens for NOAA-20 Using Yaw Measurements

JUNQIANG SUN,[1,2,*] MIKE CHU,[1,3] MENGHUA WANG[1]

[1]*NOAA National Environmental Satellite, Data, and Information Service Center for Satellite Applications and Research E/RA3, 5830 University Research Ct., College Park, MD 20740, USA*
[2]*Global Science and Technology, 7855 Walker Drive, Suite 200, MD 20770, USA*
[3]*Cooperative Institute for Research in the Atmosphere, Colorado State University, Fort Collins, CO 80523, USA*
**Corresponding author: junqiang.sun@noaa.gov*

Received XX Month XXXX; revised XX Month, XXXX; accepted XX Month XXXX; posted XX Month XXXX (Doc. ID XXXXX); published XX Month XXXX

The follow-up Visible Infrared Imaging Radiometer Suite (VIIRS) housed in the NOAA-20 satellite and the first of four in the NOAA Joint Polar Satellite System satellite series, was launched on 18 November 2017. The on-orbit satellite yaw maneuver operation was carried out on 25-26 January 2018 over 15 scheduled orbits to obtain responses of the reflective solar bands (RSBs) and the solar diffuser stability monitor (SDSM) over a specified angular range. This paper presents a comprehensive analysis of the yaw measurements that characterizes the three required input functions for the standard on-orbit RSB calibration pipeline. The characterization functions of the product of the bidirectional reflectance factors (BRFs) of the solar diffuser (SD) with the vignetting function (VF) of the SD screen (SDS), dubbed the BRF-VF-products (BVPs), are derived for the two required outgoing directions from the SD, one set for the RSB BVPs from the SD to the Rotation Telescope Assembly (RTA) that directs light to the RSBs, and another set for the SDSM BVPs for the outgoing direction from the SD to SDSM. The VFs for the attenuation screen placed in front of the Sun-view port, the Sun-view screen (SVS), are analyzed as a set of standalone functions to characterize the direct solar illumination reaching the SDSM through the SVS, but the complexity of their non-smooth two-dimensional dependence requires an additional direct treatment in the derivation of the degradation of the SD, the H-factors. The results for the RSB BVPs, SDSM BVPs and the SVS VFs are presented and discussed, and further applied to derive the early-mission performance of H-factors and the RSB calibration coefficients, or F-factors. The overall results of the H-factors and F-factors showing smooth trends with negligible residuals indicate that the derived BVP functions and the SVS VFs have been accurately characterized or treated, and are ready for use for the standard on-orbit RSB calibration of NOAA-20 VIIRS.

OCIS codes: *(280.0280) Remote sensing and sensors; (120.0120) Instrumentation, measurement, and metrology; (010.0010) Atmospheric and oceanic optics.*

http://dx.doi.org/10.1364/AO.99.099999

1. INTRODUCTION

The first of the four follow-up Visible Infrared Imaging Radiometer Suite (VIIRS) instruments, designated as NOAA-20 VIIRS, was launched on 18 November 2017. It is the first to follow the precursor VIIRS housed in the Suomi National Polar-orbiting Partnership (SNPP) satellite launched six years prior on 28 October 2011 [1]. NOAA-20 VIIRS is effectively the same built as SNPP VIIRS, comprising 14 reflective solar bands (RSBs) with 3 image bands (I1-I3) and 11 moderate bands (M1–M11) operating in the spectral region of 0.41 to 2.25 μm, 7 thermal emissive bands (TEBs) with 2 image bands (I4 and I5) and 5 moderate bands (M12–M16) operating from 3.7 to 12.013 μm, and a single panchromatic day-night band (DNB) covering 0.5 to 0.9 μm. Among the many monitoring and characterization activities in the critical post-launch testing period, one of the most important special operations prepping the instrument for the standard operational on-orbit calibration of its RSBs is the yaw-maneuver operation that provides the needed measurements of the on-orbit response of the key instrument components over an extended angular range. The comprehensive analysis of the yaw measurements for the characterization of the key input functions for the standard on-orbit RSB calibration is the focus of this work.

The strategy of the standard on-orbit calibration for NOAA-20 VIIRS is effectively identical to that of SNPP VIIRS [2]. At the core of the RSB calibration operation is a solar diffuser (SD) of near ideal reflectance property that reflects off a quantifiable amount of radiance, from the

impinging solar illumination, to the RSB detectors. An accompanying solar diffuser stability monitor (SDSM) monitors the changing reflectance performance of the SD, the so-called SD degradation, or H-factors, through regularly planned measurement operations. The characterization of the on-orbit RSB performance, or the F-factors, is straightforwardly computed by referencing the detector response to the incoming illumination from the SD, which is quantified with the input of the SDSM-measured H-factors.

The standard on-orbit RSB calibration calculation requires several additional pre-derived fixed functions to account for the various optical effects embedded within the solar illumination reaching the SD and SDSM. First, there are two open ports used for the operational on-orbit calibration of the RSBs (see Fig. 1) - the Sun-view port for illuminating the SDSM and the SD port for illuminating the SD. A pin-holed screen (a cover plate with a complex array of pin holes) is placed in front of each port for the purpose of attenuating the solar illumination to prevent detector saturation especially during the full solar illumination stage. The Sun-view screen (SVS) and the SD screen (SDS), however, impart additional optical vignetting effect to the SDSM or SD, thus requiring a vignetting function (VF) to characterize the transmittance of each screen. Second, the reflectance property of the SD, described by the four-dimensional bidirectional reflectance distribution function (BRDF), two angles for the incident light and two angles for the outgoing light, needs to be carefully characterized over the angular range required by the standard on-orbit RSB calibration for the entire mission. The BRDF is also wavelength dependent. In reality for the calibration events, the outgoing angles of light for the BRDF or the SD are fixed toward either the SDSM or the Rotating Telescope Assembly (RTA) that directs light to the RSBs, thus simplifying the characterization to a set of bidirectional reflectance factors (BRF) for two given specified outgoing directions at various wavelengths, leaving the dependence only on the two incident angles of the light to the SD. Specifically, the BRFs of the SD and the VF of the SDS are not separately characterized, but are derived together as a set of multiplicative products, the products of SD BRFs and SDS VF, dubbed as BRF-VF products (BVPs) [3], to describe the combined optical effect by the SDS and the SD for each band or detector. Because the RSBs and the SDSM are of two different outgoing directions with respect to the SD, two separate sets of BVP functions are separately derived – the SDSM BVPs for the direction toward the SDSM from the SD needed for the on-orbit calibration of the SD reflectance performance, or H-factors, and the RSB BVPs toward the direction of RTA (RSBs), for the standard on-orbit calibration of the RSBs, or F-factors. On the other hand, the VFs of the SVS are a standalone set of functions characterizing the solar illumination passing through the SVS to the SDSM.

The necessary measurements to characterize RSB BVPs, SDSM BVPs and SVS VFs may in principle be derived over a period of six months to one year with the on-orbit observations, but a specially planned yaw operation in the early mission [4] can acquire the necessary measurements at essentially one moment that are considered more reliable and easier to compute because the BRDF of the SD effectively remains constant over the very short duration of the operation. For NOAA-20 VIIRS, the yaw operation was carried out 25-26 January 2018 over 15 scheduled orbits. The yaw maneuvers tilt the spacecraft through the required angular range of the incident illumination to provide a set of one-time measurements of the response of the RSBs and the SDSM [4]. These functions are characterized once for use throughout the mission and are assumed to remain unchanged.

This work follows closely the earlier analysis done for SNPP VIIRS [3]. For RSB BVPs, differences among bands, detectors, two sides of the half-angle-mirror (HAM) and the two gain statuses, which are the high-gain (HG) and the low-gain (LG), are shown and discussed. One major difference in this analysis is that any absolute form of RSB SD BRFs, SDSM SD BRFs and the SDS VF are not presented, and no new insights into the absolute functions are gained from the NOAA-20 VIIRS analysis. However, this work presents a detailed analysis and discussion of the standalone SVS VFs and their complexity.

The organization of this paper is as follows. Section 2 briefly describes the yaw measurements and general issues of the characterization analysis. Section 3 shows the RSB BVPs and their results. Section 4 shows SDSM BVPs and their results. Section 5 presents the SVS VFs. Section 6 follows up with details of the impact on the H-factors from the inaccuracy of SVS VFs and the analysis treatments leading to H-factor improvement. F-factor results are also presented. Finally, conclusions and a summary are given in Section 7.

2. YAW MESUREMENTS AND ANALYSIS

Figure 1 is a schematic of the standard on-orbit RSB calibration showing the SD, SDSM, RTA, RSBs, and the two attenuation screens, the SVS and SDS, as the primary components. Table 1 lists some specifications for NOAA-20 VIIRS RSB and SDSM detectors [5]. The reflectance degradation of the SD, the H-factors, is measured by the SDSM through regularly planned instrument operations by comparing the detector response to the direct solar illumination through the SDSM Sun-view port with that of the illumination through the SD port reflecting off the SD. The characterization of the H-factors then enables the quantification of the illumination emanating from the SD to the RSBs, further allowing for the characterization of the detector response of the RSBs to derive the calibration coefficients, the F-factors.

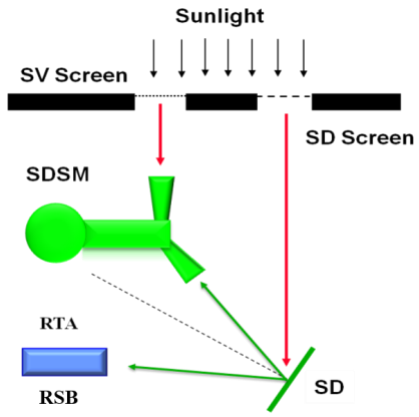

Fig. 1. VIIRS SD and SDSM calibration schematic diagram.

Table 1. Specification for NOAA-20 VIIRS RSB and SDSM detectors. All SDSM detectors are single gain and RSB detectors gain status are denoted in Column 5 as single gain or dual gain.

SDSM	CW* (nm)	RSB	CW* (nm)	Band Gain
D1	412	M1	411	DG**
D2	450	M2	445	DG
D3	488	M3	489	DG
D4	555	M4	556	DG
NA	NA	I1	642	SG***
D5	672	M5	667	DG
D6	746	M6	746	SG
D7	865	M7	868	DG
D7	865	I2	867	SG
D8	935	NA	NA	NA
NA	NA	M8	1238	SG
NA	NA	M9	1376	SG
NA	NA	M10	1604	SG
NA	NA	I3	1603	SG
NA	NA	M11	2258	SG

*CW: Center Wavelength; **DG: Dual Gain; ***SG: Single Gain

The completion of the on-orbit calibration pipeline also requires the input of the characterization functions of the impact of the vignetting effect of the two solar screens, the SVS VFs and the SDS VF, and the BRFs of the SD, all of which impart additional effects and angular dependence to the illumination reaching the SD and the SDSM. An important detail to clarify is that, while the SDS VF is a single wavelength-independent function valid for all SDSM and RSB detectors, the SVS result demonstrates clear wavelength-dependency thus requiring a set of eight SVS VFs for the SDSM detectors. The SD BRFs, for either the SDSM or the RSBs, are also a set of different functions individually considered for different bands or detectors because of the wavelength-dependence. However, the SDS VF and the SD BRFs are not individually derived, and it is instead their products, the BVPs, that are required to characterize the combined effect of the illumination going through the SDS and reflecting off the SD. Two such sets of BVPs are required – the SDSM BVPs for the direction from the SD toward the SDSM, and the RSB BVPs from the SD toward the RTA, which directs light to the RSBs. On the other hand, the SVS VFs are derived standalone since the illumination through the SDSM Sun-view port goes directly to the SDSM. Thus, one of the most critical post-launch operations is the specially planned satellite yaw maneuver designed to tilt the satellite through a sequence of rotations to obtain sensor responses of the SDSM and RSB detectors to the solar illumination over a specified angular range. The characterization of the three sets of the required functions – the SDSM BVPs, the RSB BVPs and the SVS VFs – from the yaw measurements is the focus of this analysis.

These functions depend on the direction of the solar illumination describable by two angles. Figure 2 shows the projection of a displacement vector from the instrument to the Sun in the instrument coordinate frame by the solar azimuth, solar declination, solar elevation, and solar zenith angles. Any combinations of two linearly independent solar angles, as well as in other coordinate frames, are legitimate choices. The solar azimuth and declination angles of the instrument coordinate frame are the two common choices to characterize the required functions, and solar zenith and solar elevation angles are not linearly independent coordinates given the specified sensor-Sun vector.

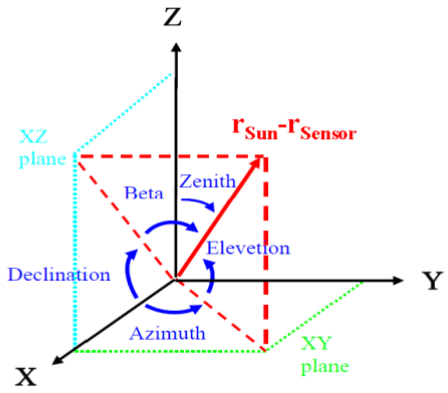

Fig. 2. Solar angles in the instrument coordinate system.

An on-orbit RSB calibration event occurs during the short interval of direct full solar illumination to the instrument components when the satellite is in position to cross the terminator from the nightside to the dayside. In general, the alignment of the sun direction with SD port moves nominally through solar declination along with the satellite motion through the orbit whereas the solar azimuth angle remains nearly unchanged within this short interval. The standard procedure uses the data from the interval of 13° to 17° in solar declination, call the "sweet spot" [6, 7], a sub-interval within the full-illumination stage that occurs just before terminator crossing, for the calculation of both the H-factors and F-factors. Nevertheless, the solar azimuth angle varies noticeably over multiple orbits but staying within a predictable range following a seasonal pattern. Thus, the dependence on solar declination angle varies through the daily orbits of the satellite around Earth, but the dependence on solar azimuth angle nominally varies through the yearly orbits of Earth and the satellite around the Sun. The satellite yaw operation therefore needs to cover the required range of solar azimuth angle to provide a set of measurements of the sensor responses, both of SDSM and the RSBs, for the purpose of characterizing the angular dependence of the three set of functions aforementioned. Figure 3 shows the solar declination angle versus solar azimuth angle for the 15 yaws on 25-26 January 2018 through the planned 15-orbit operation, but displayed only for the four-degree declination angle range of 13° to 17° of the "sweet spot." The displayed planned azimuth angular range is from 13° on the first yaw to about 31° on the final yaw, with each yaw tilts through about 1.2° in solar azimuth angle over each orbit. This 3° by 17° coverage is sufficient for a robust characterization of the three sets of the input functions. It is also clarified that the rigorous and the formal description of the solar azimuth angular range is –31° to –13° although the negative signs are often not specified for convenience.

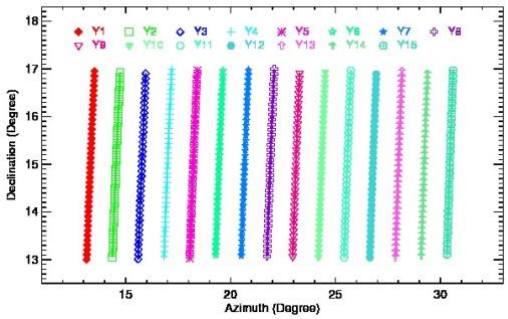

Fig. 3. Distribution of solar angles during yaw measurements for NOAA-20 VIIRS.

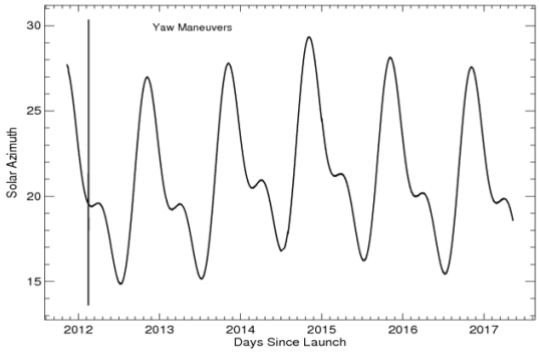

Fig. 4. SNPP VIIRS solar azimuth angle as a function of date in the instrument coordinate system. The apparent vertical line around day 110 corresponds to February 15 and 16, 2012, marking the yaw maneuvers.

The yaw planning and results for SNPP VIIRS [3, 4] can help to justify that of NOAA-20. Figure 4 shows the temporal variation of solar azimuth angle of SNPP VIIRS in the instrument coordinate frame for its first five years of mission, showing that its solar azimuth angle varies from about 15° to 30°. The apparent vertical line at day 110 is the actual planned yaw maneuver for SNPP VIIRS that took place on 15-16 February 2012 [3, 8]. It can be seen that mission-long azimuth angle variation of SNPP VIIRS remains within the range of yaw operation. Because the NOAA-20 satellite has the same orbit as that of SNPP, although trailing behind by half of orbit which is about 50 minutes, it effectively follows the same azimuth angle variation, thus justifying the planned yaw range of 13° to 31° solar azimuth angle for NOAA-20 VIIRS.

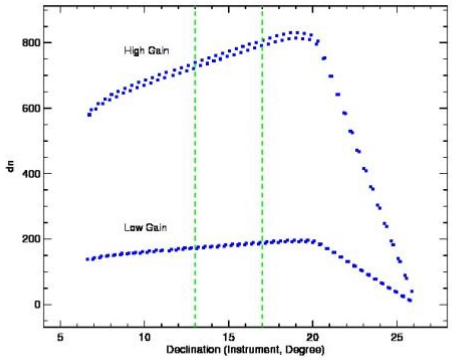

Fig. 5. Response of NOAA-20 VIIRS band M1 detector 1 to the SD view for the first yaw on 25 January 2018.

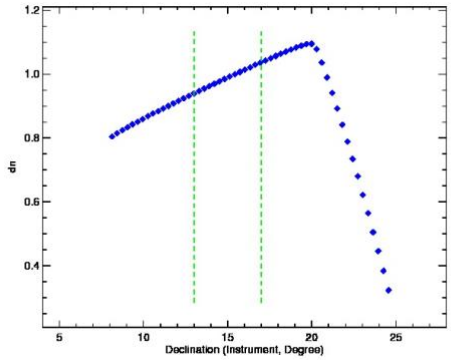

Fig. 6. Response of NOAA-20 VIIRS SDSM detector 1 to the SD view for the first yaw on 25 January 2018.

Figure 5 shows the detector response for the first yaw (Y1), in digital number (dn), of NOAA-20 VIIRS band M1 detector 1, for both HG and LG and both HAM sides, to the SD view. The 4-degree range of sweet spot is marked between the dotted vertical lines at 13° and 17° solar declination. The difference due to HAM sides is visible in the HG result although less obvious in the LG result. Each point in the figure corresponds to a single scan, which is of a full rotation of the RTA with duration of 1.779 seconds. There are about 38 scans within the sweet spot, resulting in about 9 to 10 available scans per each gain status and HAM side for a dual-gain band, and about 19 to 20 scans for each HAM side for a single-gain band. The response of the RSB detectors in the sweet spot is used for the calculation of the F-factor for each band, detector, HAM side and gain status. The corresponding SDSM detector 1 response to the SD view, also in solar declination, for the first yaw is shown Fig. 6. The sweet spot is also shown by the same 13° and 17° range in solar declination. About 38 scans are available in the sweet spot but only about 13 scans are available for the SD view because the SDSM views the SD, the Sun and the dark scene in a three-scan cycle. The response of the SDSM detectors to the Sun view in this range is used for the H-factor calculation. The corresponding SDSM detector 1 response to the SDSM Sun view for the first yaw is shown in Fig. 7, but is instead shown in solar elevation angle in the SVS coordinate system [3]. In this SVS coordinate system, the response to solar illumination is symmetric with respect to 0° solar elevation angle, with full illumination ranges from about –5° to 5°. This analysis adopts the range –2° to 2° as the

sweet spot for the Sun view, which follows the earlier SNPP VIIRS analysis convention [3, 6] but differs from the standard procedure [2] as well as those adopted in other studies [9, 10]. In this sweet spot, only one-third of the scans are available for the Sun-view as similarly described above for the SD view due to the three-scan cycle.

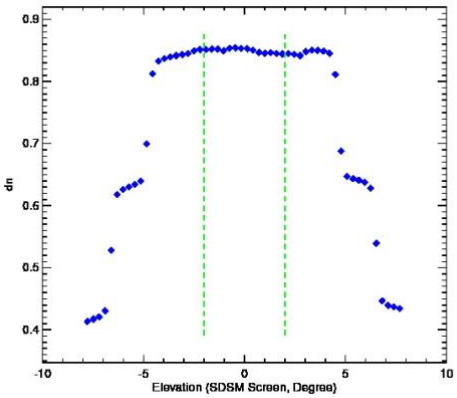

Fig. 7. Response of NOAA-20 VIIRS SDSM detector 1 to the Sun view, in the SVS coordinate system, through SDSM Sun-view port for the first yaw on 25 January 2018.

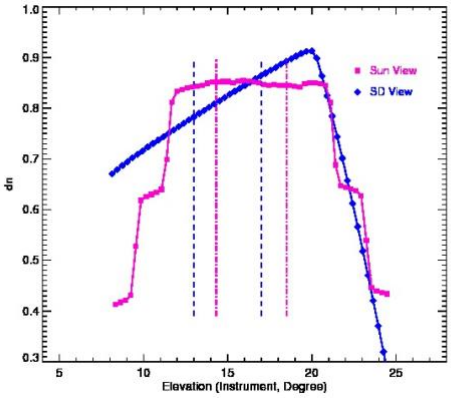

Fig. 8. Sun view (magenta squares) and SD view responses of NOAA-20 VIIRS SDSM detector 1 (blue diamonds) on 25 January 2018.

Figure 8 shows an overlay of the SDSM detector 1 response to the SDSM Sun view (magenta squares) and the SD view (blue diamonds) for the same event, demonstrating the mismatch of the two sweet spots that are as described above. In reality, the angular range of the SDSM Sun view corresponding to the fixed sweet-spot range of the SD view in solar declination varies from event to event, and may on occasions move out of the full illumination range in the SDSM Sun view, thus creating a situation with very few overlapping data points for the operational procedure [10]. The Sun and Wang [6] calibration analysis for SNPP VIIRS resolves this issue by first fixing the sweet-spot interval for the SDSM Sun-view response to −2° to 2° in the elevation angle to stay within full illumination, and further using the fixed interval for each sweet-spot, of the Sun view and the SD view, to compute the average response representing each view, thus averting the need for overlapping data points. The misalignment of the sweet spots in the two views is caused by the layout design, and the NOAA-20 VIIRS misalignment is actually smaller than that for the SNPP VIIRS [4].

3. BVPs FOR THE RSBs

The algorithm and the analysis of the RSB BVPs described here closely follow that of the SNPP VIIRS analysis by Sun and Wang [3] although numerous detailed discussions are not repeated here for NOAA-20 VIIRS. For example, the absolute form of the SDS VF and the SD BRFs are not presented here since the results do not generate new insights. It is also clarified here that many notational references for RSB is replaced by RTA for consistency with various references, such as BVP_{RTA} for RSB BVP, to explicitly denote the angular direction from the SD to the RTA.

A. Algorithms

The relationship between the incident sunlight and the instrument response for VIIRS RSBs [1, 2, 3, 11] is operationally described by a quadratic approximation,

$$L_{SD}(Sample,Scan,D,B) = F(B,D,M,G)\sum_{j=0}^{2} c_j(B,D,M,G)\, dn^j_{SD,B}(Sample,Scan,D) \quad (1)$$

where B is band number, D is the detector number of the band B, *Sample* is the sample number, *Scan* is the scan number, $L_{SD}(Sample,Scan,D,B)$ is the corresponding radiance, M is the side of the HAM at the scan, and G is the gain status of the detector at the sample of the scan. $F(B,D,M,G)$ is the calibration coefficient, the F-factor, of band B, detector D, HAM mirror side M, and gain G, and $c_0(B,D,M,G)$, $c_1(B,D,M,G)$, and $c_2(B,D,M,G)$ are temperature-effect-corrected prelaunch measured calibration coefficients [5] with a quadratic relationship between the background-subtracted instrument response and the applied radiance. The term $dn_{SD,B}$ is background-subtracted instrument response in dn.

The SD scattered sunlight radiance, on the left-hand side of Eq. (1), can also be related to the various physical parameters and the characterized functions of the instrument components as [1, 2, 3, 11], i.e.,

$$L_{SD}(Sample,Scan,D,B) = \frac{\rho_{SD,RTA}(\lambda_B)H(\lambda_B)\tau_{SDS}\cos(\theta_{SD})}{d_{ES}^2}\varepsilon_{Sun}(\lambda_B) \quad (2)$$

where $\rho_{SD,RTA}(\lambda_B)$ is pre-launch BRF with outgoing direction toward the RTA for band B, $H(\lambda_B)$ is the band-dependent SD degradation factor at the center wavelength of band B since prelaunch BRF measurement, τ_{SDS} is the VF of the SDS, θ_{SD} is the solar zenith angle to the SD, d_{ES} is the Earth-Sun distance in Astronomical Unit (AU), and $\varepsilon_{Sun}(\lambda_B)$ is solar radiance at the Earth-Sun distance of one AU. In addition to the operational description, both $\rho_{SD,RTA}(\lambda_B)$ and τ_{SDS} also have geometrical dependence describable by solar declination and solar azimuth angles, as previously discussed.

By combining Eqns. (1) and (2), a relationship between the instrument response and solar angles of the incident light can be obtained for characterizing the RSB BVP function [3],

$$BVP_{RTA}(\lambda_B) = \frac{F(B,D,M,G)}{H(\lambda_B)}\frac{d_{ES}^2}{\varepsilon_{Sun}(\lambda_B)\cos(\theta_{SD})}\sum_{j=0}^{2} c_j(B,D,M,G)\, dn^j_{SD,B}(Sample,Scan,D) \quad (3)$$

where $BVP_{RTA}(\lambda_B)$ denotes the multiplication of the $\rho_{SD,RTA}(\lambda_B)$ and τ_{SDS}, the BVP, for band B, detector D, HAM side M and gain status G. Since both $F(B,D,M,G)$ and $H(\lambda_B)$ are unknown before the RSB BVP is determined, Eqn. (3) cannot be directly used to derive the BVP functions. However, because the yaw operates through a very short time period, it is viable to assume that both coefficients have negligible

on-orbit changes to allow a relative BVP to be derived for each detector, HAM side and gain status. For the SD view, there are 48 samples for a moderate band and 96 samples for an image band in each scan, and each sample has a slightly different footprint on the SD surface due to positional and angular difference. On the other hand, $BVP_{RTA}(\lambda_B)$ does not depend on samples along scan, and hence the instrument response in Eqn. (3) is averaged over the samples. For the derivation of relative BVPs, Eqn. (3) can be rewritten as [3]

$$BVP_{RTA}(\lambda_B) \propto \frac{d_{ES}^2}{\cos(\theta_{SD})} \sum_{j=0}^{2} c_j(B,D,M,G) \left\langle dn_{SD,B}^{j}(Sample,Scan,D) \right\rangle_{Sample} , \quad \textbf{(4)}$$

where <...>$_{Sample}$ indicates averaging over samples. For convenience of discussion the right side of Eq. (4) will be referred to as the "Modified Instrument Response" (MIR) [3]. Since both BRFs and VFs should be smooth functions of two independent solar angles, the relative BVP functions for any wavelength λ can be expanded as a two-dimensional quadratic form [3],

$$BVP_{RTA}(\lambda_B) \propto a_0 + a_1\psi_V + a_2\phi_V + a_3\psi_V^2 + a_4\phi_V^2 + a_5\psi_V\phi_V , \quad \textbf{(5)}$$

where ψ_V and ϕ_V are solar declination and azimuth angles in the instrument coordinate system. The right-hand side of Eq. (5) is fitted to the measured MIR expressed in the right-hand side of Eq. (4) in a standard least-mean-square fit to obtain the six coefficients, a_0 through a_5. The relative BVPs can be fitted and derived for each band, detector, HAM side, and gain status.

In reality, the BVP functions depend only on wavelength in addition to two solar angles. They should not depend on HAM side and gain status as to be explained in the following sub-section. They may have a weak dependence on the detector due to the small optical path difference among the detectors in the same band. For comparing the BVPs obtained from different detectors, HAM sides, and gain statuses, and for assessing the uncertainty and differences, the derived two-dimensional quadratic forms are normalized at the center of the sweet spot and the azimuth angle seasonal variation range, i.e., ϕ_V = 15° and ψ_V = 22°. What is eventually required for use is a single BVP for each RSB that is independent of detector, HAM side and gain status.

The absolute form of the RSB BVPs are the required inputs for the standard on-orbit RSB calibration calculations, i.e. SD-based methodology, and can be obtained by incorporating pre-launch measurements for normalization. The analysis and discussions for the absolute forms remain effectively identical to that of SNPP VIIRS [3] and are not repeated here. All final RSB BVPs shown are of absolute form.

B. Results

Figure 9 shows the relative RSB BVP result of NOAA-20 VIIRS for four selected yaws for band M1, $BVP_{RTA}(\lambda_{M1})$ – specifically for detector 1, HAM 1 and HG – in the sweet-spot range expressed over solar declination. Each point marks one calculated relative BVP corresponding to one scan, and there are about 10 scans within the sweet-spot range for each yaw. Each curve that goes through the set of the BVP points for each yaw is taken from the two-dimensional fitted surface, and not an individual one-parameter curve fit, showing close agreement of the measured values and the fitted surface. The result shows that the fit well captures the function, with the fitting residuals being less than 0.1%.

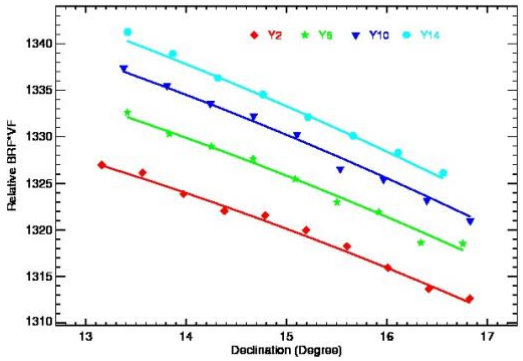

Fig. 9. Relative BVP of NOAA-20 VIIRS band M1, detector 1, HAM 1, and with high gain. Y2, Y6, Y10 and Y14 denote second, sixth, tenth and fourteenth yaw maneuver, respectively.

The RSB BVP functions are expected to be independent of detector, HAM side and gain status. Figure 10 demonstrates the detector-independence of the normalized $BVP_{RTA}(\lambda_{M1})$ at three selected azimuth angles, at –31°, –22° and –13° (or 31°, 22°, 13° when ignoring minus sign). For each of the three selected azimuth angles, the BVP points over the sweet-spot declination angle range for all 16 detectors, for HAM 1 and HG, show less than 0.1% differences. Figure 11 demonstrates the independence of HAM sides and gain statuses for the same three selected azimuth angles. The results of two HAM sides and for each of the two gain statuses at each selected azimuth angle show close agreement on the level of 0.1%. The minor differences arise from the LG result having slightly higher error, thus this analysis takes the average over all detectors and HAM sides, but using only the HG result, as the best BVP representative of each RSB.

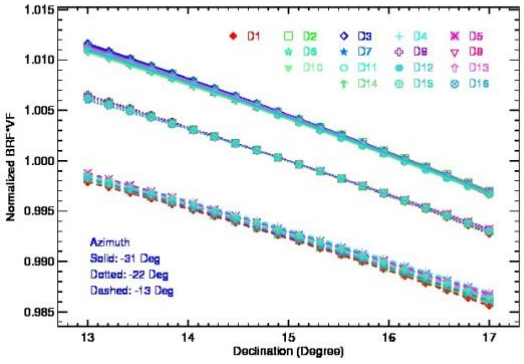

Fig. 10. Normalized BVP of NOAA-20 VIIRS band M1, HAM 1 with high gain. D1, …, D16 represent detector 1, …, detector 16, respectively.

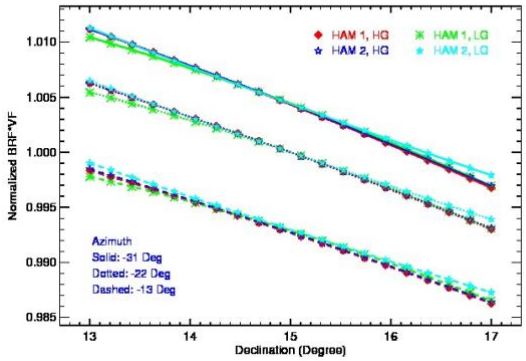

Fig. 11. Normalized detector-averaged BVP for NOAA-20 VIIRS band M1. HG and LG represent high gain and low gain, respectively. HAM 1 and HAM 2 denote HAM side 1 and HAM side 2, respectively.

The full two-dimensional surface of the detector- and HAM side-averaged of HG BVPs is shown for bands I1, M1 and M11 in Figs. 12, 13 and 14, respectively, as functions of solar declination and solar azimuth angles. All three surfaces vary smoothly over a few percent within the range shown, as for all RSB BVPs. Noticeable but minor differences in the angular dependence, or the shape of the surfaces, among the three RSB BVPs can be seen, indicating a weak wavelength-dependence in the $BVP_{RTA}(\lambda)$ over the spectral coverage of the NOAA-20 RSBs. That is, the angular dependence on the two incident angles for all RSB BVPs, which have identical fixed outgoing angle from the SD to the RTA, is very similar. Because SDS VF is in principle not dependent on wavelength, this apparent weak wavelength-dependence is attributed to the SD BRFs, which is consistent with the overall finding of this analysis. Overall, all surfaces of RSB BVPs vary about 1.0% over the displayed range of both solar declination angle and solar azimuth angle. Table 2 lists the coefficients of the quadratic form for all 14 RSB BVPs.

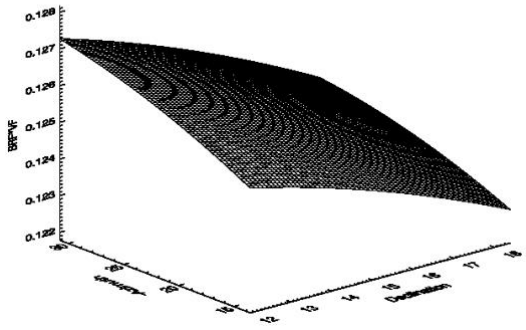

Fig. 12. Detector and HAM side-averaged of HG BVP for NOAA-20 VIIRS band I1 with respect to azimuth and declination angles in the instrument coordinate system.

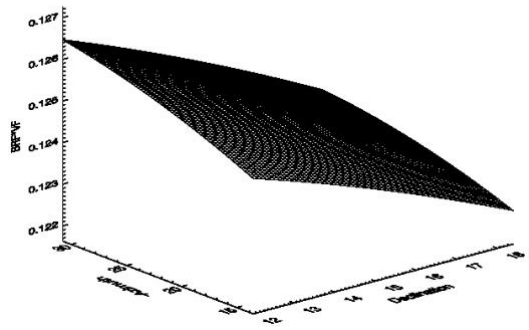

Fig. 13. Detector and HAM side-averaged HG BVP for NOAA-20 VIIRS band M1 with respect to azimuth and declination angles in the instrument coordinate system.

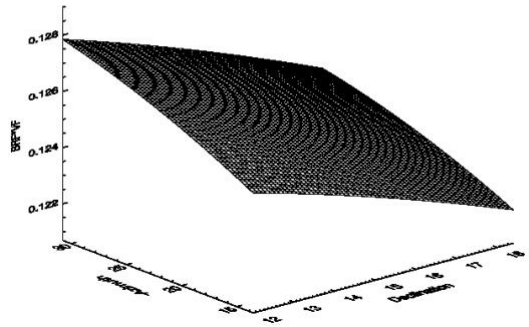

Fig. 14. Detector and HAM side-averaged HG BVP for NOAA-20 VIIRS band M11 with respect to azimuth and declination angles in the instrument coordinate system.

Table 2. Coefficients of the quadratic form for the BVPs of NOAA-20 VIIRS RSBs.

Band	a_0	a_1	a_2	a_3	a_4	a_5
I1	0.12168306	0.00030271	-0.00030411	-0.00002083	-0.00000297	0.00000429
I2	0.12455435	-0.00006957	-0.00030301	-0.00001051	-0.00000271	0.00000417
I3	0.12378343	-0.00011585	-0.00036866	-0.00000842	-0.00000351	0.00000443
M1	0.12431499	-0.00000644	-0.00023866	-0.00001064	-0.00000226	0.00000389
M2	0.12384790	0.00005314	-0.00025704	-0.00001279	-0.00000256	0.00000386
M3	0.12433026	-0.00000718	-0.00027091	-0.00001086	-0.00000268	0.00000395
M4	0.12395062	0.00002823	-0.00028726	-0.00001223	-0.00000283	0.00000413
M5	0.12404792	0.00000883	-0.00030830	-0.00001184	-0.00000303	0.00000416
M6	0.12363595	0.00003249	-0.00032228	-0.00001243	-0.00000304	0.00000463
M7	0.12346949	0.00001500	-0.00032293	-0.00001212	-0.00000295	0.00000459
M8	0.12121013	0.00021903	-0.00036930	-0.00001865	-0.00000344	0.00000490
M9	0.12230603	0.00005675	-0.00037001	-0.00001391	-0.00000370	0.00000377
M10	0.12285558	0.00000771	-0.00036314	-0.00001227	-0.00000346	0.00000415
M11	0.12355106	-0.00002258	-0.00035874	-0.00001336	-0.00000328	0.00000388

4. BVPs FOR THE SDSM DETECTORS

This section presents the algorithms for the derivation of the BVPs for the SDSM detectors and the results. In parallel with the RSB BVP effort described above, the relative form of the SDSM BVPs are first analyzed and then normalized to pre-launch measurements.

A. Algorithms

For SDSM, the relationship between the incident sunlight and the SDSM response is characterized by a linear relationship [1, 2, 3, 11], i.e.,

$$L_{SD}(Sample, Scan, D) = Q(D) dc_{SD,D}(Sample, Scan) \quad (6)$$

where *Sample* and *D* are the SDSM sample number and detector number, respectively. $L_{SD}(Sample,Scan,D)$ is the radiance at the sample of the scan observed by SDSM detector *D*, and $Q(D)$ is calibration coefficient of SDSM detector *D*, which is inversely proportional to the gain of the detector. The term $dc_{SD,D}(Sample,Scan)$ is the background-subtracted SDSM response for the SD view. Similar to the RSBs as described previously, the SD scattered sunlight radiance on left-hand side of Eqn. (6) is related to other physical parameters for SDSM detector *D* as [3]

$$L_{SD}(Sample,Scan,D) = \frac{\rho_{SD,SDSM}(\lambda_D) H(\lambda_D) \tau_{SDS} \cos(\theta_{SD})}{d_{ES}^2} \varepsilon_{Sun}(\lambda_D) \quad (7)$$

where λ_D is the center wavelength of the SDSM detector *D*, $\rho_{SD,SDSM}(\lambda_D)$ is the measured pre-launch BRF with outgoing direction toward the SDSM for detector *D*, and the remaining physical parameters are as previously explained. It is particularly noted here that $\rho_{SD,SDSM}(\lambda_D)$ is different from the previously discussed $\rho_{SD,RTA}(\lambda_B)$ because the outgoing directions are different for the RTA and the SDSM from the SD. In a similar situation as for RSB BVPs described above, Eqns. (6) and (7) can be combined to isolate the BVP function for SDSM detector D, but cannot be used directly because $Q(D)$ for SDSM detector *D* is also unknown. Thus, only the relative BVP for SDSM detector *D* can be derived from the yaw measurements [3], i.e.,

$$BVP_{SDSM}(\lambda_D) \propto \frac{d_{ES}^2}{\cos(\theta_{SD})} \left\langle dc_{SD,D}(Sample, scan) \right\rangle_{Sample} \quad (8)$$

where $\langle \ldots \rangle_{Sample}$ indicates the average over the SDSM samples. The dependence of the SDSM BVPs on the two solar angles can similarly be expanded into a two-dimensional quadratic form [3],

$$BVP_{SDSM}(\lambda_D) \propto a'_0 + a'_1 \psi_V + a'_2 \phi_V + a'_3 \psi_V^2 + a'_4 \phi_V^2 + a'_5 \psi_V \phi_V \quad (9)$$

and be fitted with the values calculated from the right side of Eq. (8). The absolute form of $BVP_{SDSM}(\lambda_D)$ can be determined by comparing the relative BVP and the prelaunch measured BVP results [3], but is actually not necessary since the H-factors are always normalized to the first measurement. Nevertheless, the final results of all SDSM BVPs are shown in absolute form.

B. Results and Comparison with RSB BVPs

Figure 15 shows the relative BVP of the SDSM detector 1, $BVP_{SDSM}(\lambda_{D1})$, for four selected yaws (Y2, Y6, Y10 and Y14), corresponding to the RSB result of Fig. 9. Each point marks one calculated relative SDSM BVP corresponding to one scan, and there are about 12 scans within the angular range of the sweet spot for each yaw. Each curve that goes through the one set of the BVP points of each yaw is taken from the two-dimensional fitted surface, showing close agreement of the measured values and the fitted surface. The residuals are less than 0.1%.

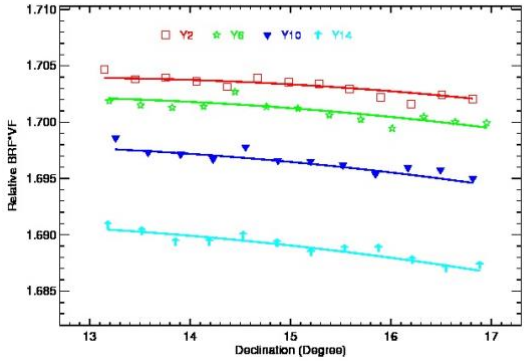

Fig. 15. Relative BVP of NOAA-20 VIIRS SDSM detector 1.

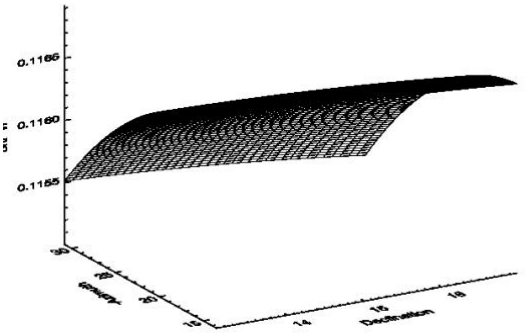

Fig. 16. BVP for NOAA-20 SDSM detector 1 with respect to azimuth and declination angles in the instrument coordinate system.

Figures 16 shows the two-dimensional surface of normalized fitted SDSM BVP for detector 1, $BVP_{SDSM}(\lambda_{D1})$, over solar declination and azimuth angles. The $BVP_{SDSM}(\lambda_{D1})$ surface can be seen to be smooth, varying about 1.0% over solar azimuth angle but only about 0.1% over solar declination. In comparison with $BVP_{RTA}(\lambda_{M1})$ at 412 nm shown previously in Fig. 13, $BVP_{SDSM}(\lambda_{D1})$ at 412 nm shown in Fig. 16 can be seen to exhibit a different shape. The difference between the angular dependence of the $BVP_{RTA}(\lambda)$ and $BVP_{SDSM}(\lambda)$ at the same λ arises from the different outgoing angles in the two respective SD BRFs, the former from the SD to the RTA (RSBs) and the latter from the SD to the SDSM, thus explicitly demonstrating the non-equivalence of the SD BRFs fixed at two difference outgoing angles.

Figure 17 shows the SDSM BVPs for detector 8, $BVP_{SDSM}(\lambda_{D8})$, which demonstrates also a smooth surface but with greater curvature over solar azimuth angle than that over solar declination angle. The two BVPs for SDSM detector 1 and detector 8, in Figs. 16 and 17, clearly show different angular-dependence as well. In this case with incident and outgoing angles of SD BRFs being equal, the difference in the angular dependence, with SDSM detector 1 at 412 nm and detector 8 at 935 nm, arises from the wavelength-dependence in $BVP_{SDSM}(\lambda_D)$. This SDSM result corresponds to that of RSB BVPs discussed above showing weak dependence on wavelength, as shown in Figs. 12–14, but with stronger dependence on wavelength. The stronger dependence of the SDSM BVPs on wavelength is attributed also to the functional behavior of the

SD BRFs at the outgoing angle from the SD to the SDSM since the SDS VF, as already discussed above for the case of RSB BVPs, is wavelength-independent. Table 3 lists the coefficients of the quadratic from for the eight SDSM BVPs.

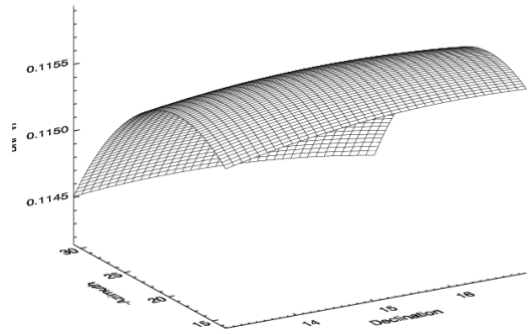

Fig. 17. BVP for NOAA-20 SDSM detector 8 with respect to azimuth and declination angles in the instrument coordinate system.

Table 3. Coefficients of the quadratic form for the BVPs of the NOAA-20 VIIRS SDSM detectors.

Detector	a0	a1	a2	a3	a4	a5
D1	0.12341792	0.00021789	0.00013406	-0.00000760	-0.00000410	-0.00000177
D2	0.12107564	0.00050558	0.00012828	-0.00001705	-0.00000399	-0.00000167
D3	0.12098229	0.00051088	0.00012474	-0.00001711	-0.00000404	-0.00000127
D4	0.12136221	0.00040071	0.00012331	-0.00001322	-0.00000395	-0.00000144
D5	0.12041843	0.00051680	0.00014304	-0.00001666	-0.00000430	-0.00000168
D6	0.12004405	0.00055752	0.00016422	-0.00001738	-0.00000457	-0.00000216
D7	0.11797024	0.00068566	0.00026063	-0.00002013	-0.00000607	-0.00000375
D8	0.11621702	0.00079842	0.00035595	-0.00002272	-0.00000783	-0.00000470

The combined results of the different angular dependence on the incident solar illumination between the two sets of BVPs and the stronger wavelength-dependence in the SDSM BVPs for the angular direction from the SD to the SDSM reveal already the complexity in the SD BRFs. The different degradation rates of the SD at the two outgoing directions, which results in so-called nonunifromity effect of the SD degradation and induces a long-term bias in the F-factors derived from the SD/SDSM calibration, has already been proven for SNPP VIIRS [12, 13, 14] and the MODerate-resolution Imaging Spectroradiometer (MODIS) on Terra and Aqua satellites [14, 15, 16]. As there is no compelling reason to expect NOAA-20 VIIRS RSBs to follow the standard calibration methodology without generating similar error as in SNPP VIIRS and MODIS that comes from the nonuniformity effect of SD degradation, the mitigation of the RSB SD/SDSM calibration error for NOAA-20 VIIRS will therefore be critically important as well.

5. SDSM SUN VIEW SCREEN VFs

This section describes the characterization of the SVS VFs, which account for the vignetting effect of the attenuation screen in front of the SDSM Sun-view port. The SVS VFs are a set of standalone functions that do not involve other calibration components since the solar illumination through the Sun-view port and the SVS goes directly to the SDSM. But unlike the SDS VF, which is in principle a single function that is consistent with the overall result, the SVS VFs are a set of eight functions for the SDSM detectors because of the apparent wavelength-dependence.

A. Algorithms

The measured responses of the SDSM detectors to the illumination through the SVS are straightforwardly proportional to the transmittance of the screen, but the SVS VFs are in reality not smooth functions. In the case of the SDS VF and RSB BVPs, because the SD, and the illumination from it, is out of focus with respect to the RTA (RSBs) and SDSM, any sharpness in the illumination due to the screen pinholes is blurred and smoothed out, resulting in both RSB and SDSM BVPs being smooth. However, for the SDSM SVS, the illumination pattern remains sharp due to the illumination source, the Sun, being effectively at infinity. The SVS VFs, therefore, will retain the sharpness due to the pinholes and fail the description of smooth functions. Furthermore, the yaw measurements implemented only at 15 selected solar azimuth angles are not sufficient to trace out the complexity of the SVS VFs. The range of the two solar angles is solar elevation angle from -2° to 2° and solar azimuth angle from -14.5° to 1.7° in the SDSM SVS coordinate system; this corresponds nominally, but not of exact match as previously discussed, to the solar declination angle from 13° to 17° and the solar azimuth angle from 13° to 31° in the instrument coordinate system. While the yaw operation generates about 14 measured points in Sun view over the solar elevation angle of a narrow 4-degree range, it provides only 15 yaws (measured points) for the solar azimuth angle range over a much wider 16-degree range. A matrix of numerical interpolation is instead used for the description of the transmittance as an initial reference for further necessary analysis or treatment.

The procedure of the interpolation is presented as follows. A matrix of dimension 51 by 51 is used to hold the interpolation of the yaw data to describe the dependence on solar elevation and azimuth angles in the SVS coordinate system. For each of the 15 yaws in the range of the solar elevation angle from -2° to 2°, 51 evenly distributed points are selected for interpolation. All 15 yaws contain the same distribution of 51 elevation angles. Within each yaw, for a given selected elevation angle, the azimuth angle and the SDSM response is linearly interpolated using the data from the two nearest yaw measurements to the given solar declination. The interpolation then, for each of the 51 solar elevation angles, extends cross-yaw along one solar elevation angle in the range of the solar azimuth angle from -14.5° to 1.7° also for 51 evenly distributed solar azimuth angles. For any given selected solar azimuth angle along the solar elevation angle, the instrument response is further interpolated using the two nearest solar elevation angles and their associated interpolated instrument responses.

B. Sun View Screen VFs for the SDSM Detectors

Figures 18, 19 and 20 show the interpolated results for SVS VFs for SDSM detectors 1, 6 and 8, respectively. It can be seen the VF results are not smooth, demonstrating clearly the complexity from the effect of pinhole array. The SVS VFs for SDSM detectors 1–6 are similar to one another, whereas the VFs of detectors 7 and 8 are more complex. The dependence along solar azimuth angle can be seen to show greater variation than that along solar elevation angle. However, the yaw maneuver actually does not provide sufficient measurements to capture the complexity of the SVS VFs, and thus the actual VFs for the SDSM detectors are more complex than what can be characterized and shown in Figs. 18–20. The current state of the analysis procedure and available data is unable to further handle the resulting inaccuracy in the interpolated SVS VFs directly, and

necessarily must go through H-factor results for direct treatment, as to be shown below.

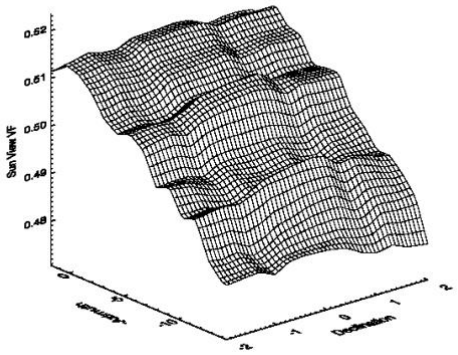

Fig. 18. Interpolated VF for NOAA-20 SDSM Sun-view port screen observed by SDSM detector 1.

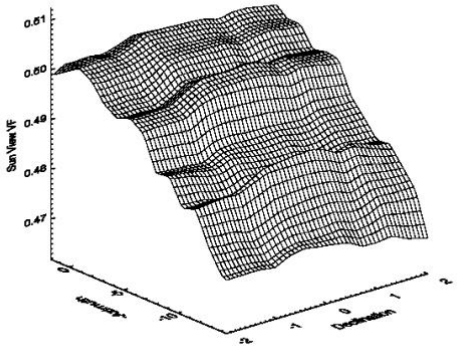

Fig. 19. Interpolated VF for NOAA-20 SDSM Sun-view port screen observed by SDSM detector 6.

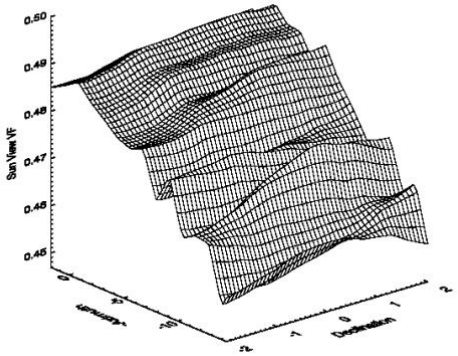

Fig. 20. Interpolated VF for NOAA-20 SDSM Sun-view port screen observed by SDSM detector 8.

The differences among the SVS VF results, including small but observable differences between that of detector 1 and 6, reveal a dependence on wavelength contrary to the expectation that the vignetting effect should be wavelength-independent. Further investigation into this complication is not within the scope of this work, but the practical approach adopted here and the main goal to characterize the effect of the SVS VFs need not be concerned with this complication. The analysis simply adopts to treat each SVS VF and its wavelength-dependence effect individually.

6. PERFORMANCE AND FURTHER IMPROVEMENT

The derived H-Factors and F-Factors are shown in this section to demonstrate the performance of the three sets of the characterized functions. Inaccuracy in the SVS VFs manifested in the H-factors are further analyzed and characterized. For notational convenience, detectors will be denoted by the capital letter D follow by the corresponding number, such as D1 for detector 1, D2 for detector 2, and so on.

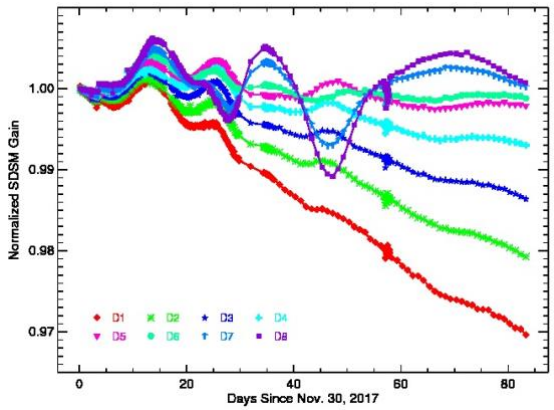

Fig. 21. Early-mission NOAA-20 SD degradation (H-Factors), original.

A. H-Factors

Figure 21 shows the eight H-Factors, one for each SDSM detector, derived with SDSM BVPs and the interpolated SVS VFs. Expectedly, errors in the H-factors in the form of artificial oscillation arise from the inaccuracy of the SVS VFs. This is confirmed by a comparison of the SDSM responses to the SD view and the Sun view. Figure 22 shows the responses of the SDSM to the SD view, corrected for the inverse-square of the Sun-Earth distance and the solar angle effect by the BVPs as described in Eq. (2), which is the product of both the SD degradation and the SDSM detector degradation. The responses are smooth functions of time apart from some small features due to the SDSM detector gain changes or other on-orbit operations during the early mission. This result indicates that both SD and SDSM degrade smoothly. Figure 23 shows the response of the SDSM to the Sun view, also corrected for SVS VFs and Sun-Earth distance effect as described in Eq. (3), which represents the SDSM detector degradation. Different from the SD view responses, the Sun-view result indeed exhibits significant modulating features. The artificial features in the SDSM Sun-view responses are attributed to the inaccuracy in the interpolated SVS VFs. Interestingly, the two results exhibit many of the same discontinuities and jumps, indicating these minor features to be specific to SDSM responses arising from gain adjustments or various operational activities in the early mission. The H-factors in Fig. 21 also do not exhibit these features of small jumps or discontinuities, proving the expected cancellation of these effects that are not related to the SD degradation.

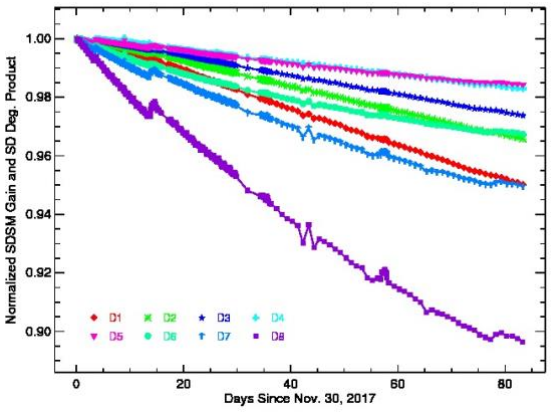

Fig. 22. NOAA-20 SDSM SD view response.

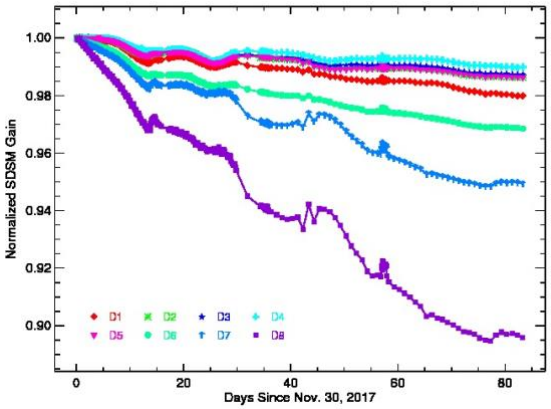

Fig. 23. NOAA-20 SDSM Sun-view response.

There are some strategies that can be used to improve the accuracy of the SVS VFs or the H-factor results. The most direct and obvious one is to extend the yaw measurement operation to improve SVS VFs. However, the required extended on-orbit operation over many more days is an expensive proposition. A quick estimate to reduce uncertainty, for example from 1% to 0.25%, by increasing the number of measurements along solar azimuth angle places the required yaws to be close to 60, assuming that the error is proportional to the quantity of yaws.

Also, because pinholes are evenly distributed along the two angular coordinates, it is reasonable to assume that the most cost-effective condition is to match the measurement density along the two directions. The density of measurement along solar elevation angle is fixed by the 13 or 14 available scans in the sweet spot for the Sun view over the 4-degree range, or 3-plus measurements per degree. Thus, for the 18-degree range over solar azimuth angle to have the same measurement density then requires about 60 measurements. These two different considerations reach a similar conclusion. Still, while 60 yaws are definitively costly, the estimated 0.25% error still remains larger than the expected error of 0.1% such as already achieved by SNPP VIIRS [6].

A more practical approach is to wait for half year or longer for the instrument to cover on its own over the entire range of solar azimuth angle to obtain a sufficient set of measurements. This is nearly equivalent to extending the yaw operation in obtaining a higher number of measurements over the required angular range, except that significant SD and SDSM degradation over the six-month period or longer adds an additional complication – that the analysis of the six-month data must account for the degrading performance of the SD and SDSM while simultaneously deriving the SVS VFs. Certainly, the half-year or longer waiting period is another undesirable drawback of this approach. It is important to reiterate that the non-smooth surface of SVS VFs are beyond the standard fitting approach to characterize. Thus for any realistic yaw operation or extended time approach, numerical interpolation to characterize the SVS VFs remains as only meaningful result even if not accurate.

This analysis adopts another approach that takes advantage of the currently available data for the interpolative approach to derive the H-factors without needing to wait for further data. Because the interpolative approach requires only the local information to derive the SDS VF values for any given time, any single SDSM calibration event, in reality, is correspondingly dependent on the local information as well. That is, at a given solar elevation and solar azimuth angles, only the data closest to the set of solar angles are used, and any inaccuracy in the resulting local SVS VF values will manifest in the derived H-factors. Because the interpolated SVS VF surfaces are unambiguously constructed, the errors between the interpolated SVS VFs and the true functions are, in principle, themselves well-defined two-dimensional functions of the solar angles. Therefore, the error in the H-factors due to SVS VF inaccuracy will be correlated with the solar angles. The challenge is finding a usable description of the correlation, or using it correctly, so that the effect impacting the H-factors sourcing to the SVS VF inaccuracy can be characterized.

Since the behavior of the SVS VFs for SDSM D1 through D6 is similar, it is assumed in the first approximation that the impact of the SVS VF inaccuracy on the H-factors should be similar for these six detectors. The H-factor results in Fig. 21 show their similarity. The error characterized from one chosen H-factor should be applicable to the other five for removal. This approach thus does not further analyze SVS VFs directly, but instead uses the H-factors to account for the effect of the inaccuracy SVS VFs, through a straightforward fitting scheme to directly characterize the error in the H-factors. The treatment for SDSM D7 and D8 is handled differently, since their SVS VFs behave differently, and the modulation in their H-factors as shown in Fig. 21 are significantly more dramatic. However, these two detectors of the longest wavelengths among the eight SDSM detectors are expected to have the least degradation, consistent with the pattern of degradation seen in Fig. 21, even though they exhibit the greatest modulation. A simple and straightforward fitting suffices for these two detectors, provided that the assumption of having the least degradation is correct.

The yaw operation, although not adequate for the accurate characterization of SVS VFs, does provide a critical initial set of measurements to allow a set of usable interpolated SVS VFs to be constructed. This is very beneficial, if not indispensable, to derive the initial H-factors with a reasonable level of accuracy at only about 1%, which allows further improvement. This third approach is equivalent to the one waiting out another six-month period or longer after the yaw operation, but without further waiting, because of the nature of the locality of the interpolated approach. The inaccuracy of the interpolated SVS VFs can be directly treated in the H-factors, with the understanding that these errors in the H-factors are correlated with the solar angles and hence of a definitive pattern for the all detectors in general, and can be straightforwardly characterized.

The specific steps of the local fitting approach using H-factors for D1 through D6 are described as follows. The H-factors of SDSM D5 and D6 are selected for characterization of the modulating pattern since they are the most stable among all without significant degradation. The ratios of the measured and the fitted H-factors, assumed in the first approximation to be effectively independent of wavelength although

small deviations may remain, are built to represent the effect of the modulation in D1 through D6. Specifically, it is empirically found that characterization from D6 is more applicable to D1, and that from D5 is more suited for D2, D3 and D4. In any case, using D5 and D6 characterization amounts to at most 0.2% difference, and this combined use of the two characterizations is adopted simply for the optimal result. The improved H-factors are calculated by dividing the original H-factors by the ratios to remove the modulation. The improved H-factors for D1 through D6 displayed in Fig. 24 indeed show significantly improved stability with remaining error on the order of 0.1%, consistent with SD degradation being smooth with time. It has already been noted that the SVS VFs exhibit some minor wavelength dependency that is contrary to expectation, and the improved result using D5 and D6 indeed demonstrates the existence of some minor wavelength-dependent effect. Nevertheless, the improved H-factors easily reveal the smooth underlying trend. An exponential-quadratic fit is further applied to each of the six improved H-factors individually.

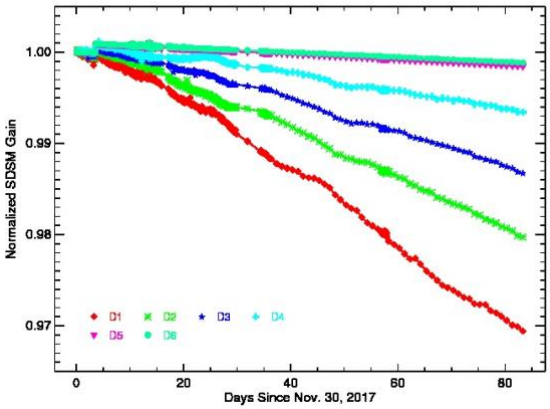

Fig. 24. Early-mission NOAA-20 SD degradation (H-Factors), improved.

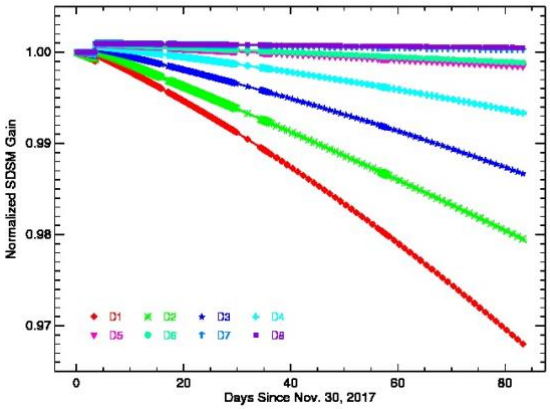

Fig. 25. Early-mission NOAA-20 SD degradation (H-Factors), fitted.

Figure 25 shows the fitted H-factor result for all eight SDSM detectors. The H-factors for the first six detectors are analyzed as just described above. The H-factors of SDSM D7 and D8 are directly fitted to an exponential-linear function as also explained prior. This is the final H-factor set to be used for the NOAA-20 VIIRS RSB SD calibration.

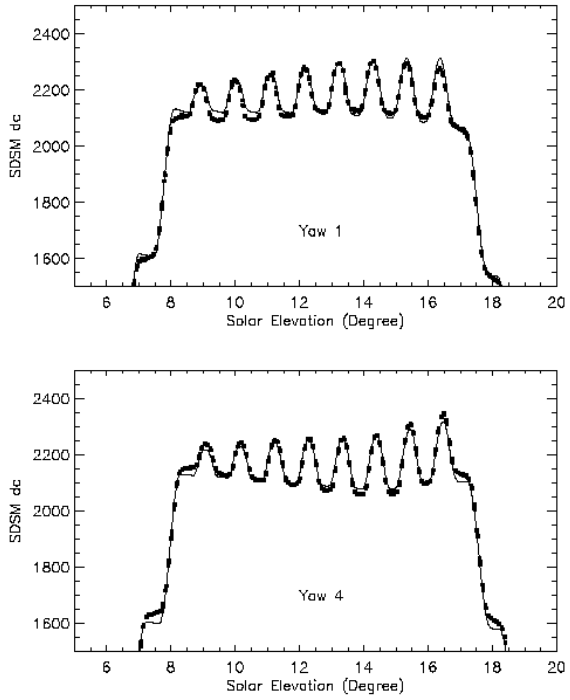

Fig. 26. Terra SDSM Sun-view responses with symbols representing measurements observed by SDSM detector 8 on April 26, 2000 and solid lines representing simulated result.

B. Simulation of the SDSM SVS VFs

A modeling approach using simulation to describe the details of the SVS and the associated optical effects may be the best approach to fully characterize the two-dimensional SVS VF surfaces. Sun et al. [17] has demonstrated for the twin MODIS a successful simulated study of the dependence of the SVS VFs on solar elevation and solar azimuth angles. Figure 26 shows the comparison result of the Terra MODIS yaw measurements and the simulated result for SDSM D8, for the first and the fourth yaw carried out on 26 April 2000. The effect of the SVS, in the form of spikes, is of the order 10 to 15% for MODIS. FOR NOAA-20 VIIRS, the corresponding effect is only about 2% as shown in Fig. 7. The yaw measurements for MODIS are also denser along solar elevation angle due to its folder mirror being fixed on the Sun view – VIIRS can also obtain the same density along solar elevation angle by similarly fixing the folder mirror position instead of maintaining the three-scan cycle during yaw operation. It is seen that the simulated result well matches the sharp spikes of the SVS VFs for the two yaws displayed. Figure 27 displays the two-dimensional simulated SVS VF result for MODIS SDSM D8, demonstrating the full complexity along both solar elevation and azimuth angles. As mentioned above, Terra MODIS SDSM SVS VFs have much complex surfaces than NOAA-20 VIIRS SDSM SVS VFs, and thus the yaw operation for MODIS definitively cannot provide sufficient measurements along both solar azimuth and solar elevation angles for the characterization of the SVS VFs. Further treatment has to be directly applied to remove the artificial oscillations in the derived SD degradation. The treatment for the MODIS SD degradation is similar to the procedure described here for NOAA-20 VIIRS.

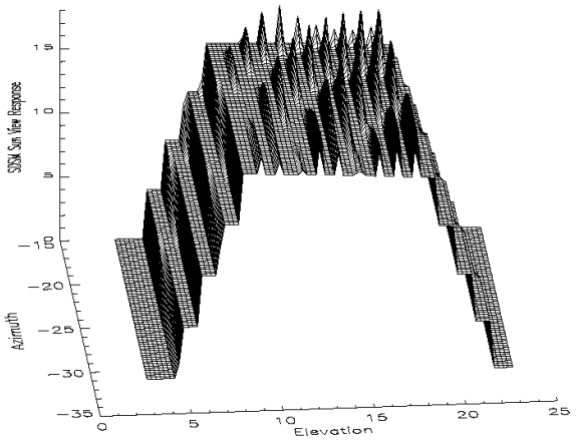

Fig. 27. Simulated 2-dimenstional Terra MODIS SDSM Sun-view screen VF.

Additionally, this MODIS simulation study revealed also the wrong installation of the SDSM in both Terra and Aqua MODIS, which was later confirmed, and that the high complexity of the MODIS SDSM SVS VFs was mainly induced by the wrong installation. In principle, the SVS VFs can be made perfectly smooth with the correct design, make and installation of the SVS and the associated components along the optical path. But because the aforementioned aspects can easily be imperfect to induce complex behavior of the SVS VFs, simulation becomes a valuable and powerful tool for modeling the calibration components and the associated effects and for providing an accurate description of the SVS VFs that captures the complexity. It is definitively a worthy future pursuit to conduct simulation studies for both SNPP and NOAA-20 VIIRs to provide an accurate description of the SVS VFs.

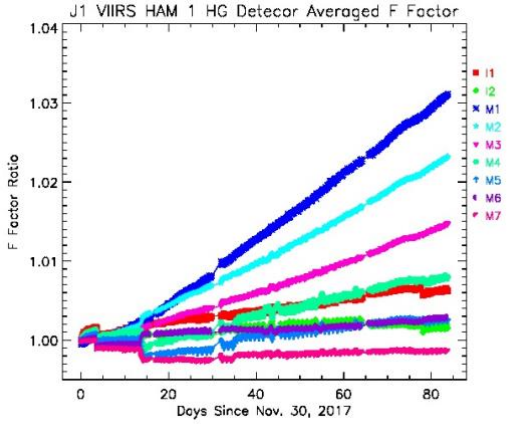

Fig. 28. Early-mission NOAA-20 VIIRS RSB F-Factors without H-Factors applied.

C. F-Factors

Figures 28 and 29 show the F-factors for the RSBs of the visible and near-infrared spectral range with and without H-factors applied, respectively. Each point of the F-factor plot is derived from each orbit as the direct measured result without any smoothing or averaging scheme. The numerous discontinuities in the trends come from the various instrument events, including some errors in the reported solar angle data and various instrument operations in the early mission affecting the RSBs. The noises are less than 0.1%.

In Fig. 28, the F-factors without the application of H-factors, thus not removing the effect of SD degradation, show smooth and stable trends with no artificial oscillations or other significant deviating features. This further confirms that the degradation of SD, as embedded within the uncorrected F-factors, to be smooth with time. This is consistent with the results above discussed for SDSM SD view responses in Fig. 22, that the H-factors should be smooth and the modulating features in the H-factors are artificial. The analysis approach for the H-factors and their eventual smooth results are therefore valid and proper.

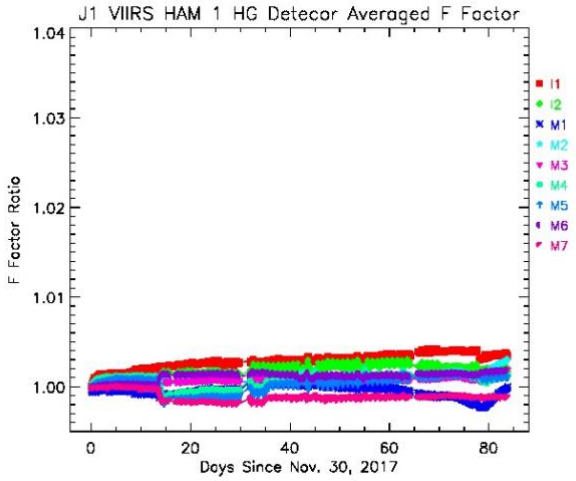

Fig. 29. Early-mission NOAA-20 VIIRS RSB F-Factors with H-Factors applied.

In Fig. 29, the H-factors are applied to remove the effect of SD degradation in F-factors, and the result exhibits the surprising performance stability of NOAA-20 VIIRS RSBs with no real band performance degradation, with the strongest level of change at only about 0.3%. This demonstrated stability by the NOAA-20 VIIRS RSBs is dramatically different than that of SNPP VIIRS RSBs which show very significant change in its early period especially for those bands of longer wavelength. For example, F-factors of SNPP VIIRS M5, M6 and M7 rise up to 8%, 15% and 35%, respectively, in the first three months [7, 18].

The overall results, in particular, in the smoothness of the H-factor as shown in Figs. 24 and 25 and F-factors as shown in Figs. 28 and 29, indicate that the BVPs for both RSB view and SDSM view have been very well characterized and that the SVS VF complexity have been correctly treated.

6. CONCLUSIONS

The RSB BVPs, SDSM BVPs and the SVS VFs, the three required sets of input functions to the on-orbit RSB calibration pipeline, for NOAA-20 VIIRS have been characterized using the yaw maneuver measurements carried out over 15 scheduled orbits on 25-26 January 2018. Each RSB is represented by a single BVP obtained by averaging over detectors and HAM sides, but using only the high-gain result for better reliability. While the RSB and SDSM BVPs are shown to be smooth and well characterized, the SVS VFs, the vignetting functions for the attenuation screen of the SDSM Sun-view port, are expectedly more complex than what can be characterized by the interpolation of the yaw

measurements. But a direct treatment of the H-factor results successfully removes the artificial oscillatory features arising from the inaccuracy of the interpolated SVS VFs. The final F-factors derived for the early mission are smooth and without artificial modulation, and surprisingly demonstrate a stable performance with changes no worse than ≅0.3% in the first three months where the greatest degradation is expected. The overall result indicates that the all BVPs have been robustly characterized and that the SVS VFs have been successfully treated, and are ready for use for the on-orbit RSB calibration of NOAA-20 VIIRS.

Funding Information. National Oceanic and Atmospheric Administration (NOAA) and National Aeronautics and Space Administration (NASA) Joint Polar Satellite System.

Acknowledgment. The views, opinions, and findings contained in this paper are those of the authors and should not be construed as an official NOAA or U.S. Government position, policy, or decision.

References

1. C. Cao, F. Deluccia, X. Xiong, R. Wolfe, and F. Weng, "Early on-orbit performance of the Visible Infrared Imaging Radiometer Suite (VIIRS) onboard the Suomi National Polar-orbiting Partnership (S-NPP) satellite," IEEE Trans. Geosci. Remote Sens., 52, 1142–1156 (2014).
2. S. Mills, VIIRS Radiometric Calibration Algorithm Theoretical Basis Document, Doc. No.: D43777 (Northrop Grumman Aerospace Systems, 2010).
3. J. Sun and M. Wang, "On-orbit characterization of the VIIRS solar diffuser and solar diffuser screen," Appl. Opt. 54, 236–252 (2015).
4. J. Sun, and X. Xiong, "Solar and lunar observation planning for Earth-observing sensor," Proc. SPIE, 8176, 817610 (2011).
5. H. Oudrari 1, J. McIntire, X. Xiong, J. Butler, Q. Ji, T. Schwarting, S. Lee, and B. Efremova, " JPSS-1 VIIRS Radiometric Characterization and Calibration Based on Pre-Launch Testing," Remote Sens. 2016, 8, 41, 1-20 (2016).
6. J. Sun and M. Wang, "Visible Infrared imaging radiometer suite solar diffuser calibration and its challenges using solar diffuser stability monitor", Appl. Opt. 53, 8571-8584 (2014).
7. J. Sun and M. Wang, "On-orbit calibration of the Visible Infrared Imaging Radiometer Suite reflective solar bands and its challenges using a solar diffuser," Appl. Opt. 54, 7210-7223 (2015).
8. J. McIntire, D. Moyer, B. Efremova, H. Oudrari, X. Xiaoxiong, "On-orbit characterization of S-NPP VIIRS transmission functions", IEEE Trans. Geosci. Remote Sens. 53, 2354-2365 (2015).
9. E. Hass, D. Moyer, F. DeLuccia, K. Rausch, J. Fulbright, "VIIRS solar diffuser bidirectional reflectance distribution function (BRDF) degradation factor operational trending and update," Proc. SPIE, 8510, 851016 (2012).
10. J. Fulbright, N. Lei, K. Chiang, X. Xiong, "Characterization and performance of the Suomi-NPP VIIRS solar diffuser stability monitor.," Proc. SPIE, 8510, 851015 (2012).
11. X. Xiong, J. Butler, K. Chiang, B. Efremova, J. Fulbright, N. Lei, J. McIntire, H. Oudrari, J. Sun, Z. Wang, "VIIRS on-orbit calibration methodology and performance," J. Geophys. Res. Atmos. 119, 5065–5078 (2014).
12. J. Sun and M. Wang, "Radiometric calibration of the visible infrared imaging radiometer suite reflective solar bands with robust characterizations and hybrid calibration coefficients," Appl. Opt., 54, 9331-9342 (2015).
13. J. Sun and M. Wang, "VIIRS reflective solar bands calibration progress and its impact on ocean color products", Remote Sens. 8, 194 (2016).
14. J. Sun, M. Chu and M. Wang, "Degradation nonuniformity in the solar diffuser bidirectional reflectance distribution function," Appl. Opt. 55, 6001-6016 (2016).
15. J. Sun, X. Xiong, A. Angal, H. Chen, A. Wu, and X. Geng, "Time dependent response versus scan angle for MODIS reflective solar bands," IEEE Trans. Geosci. Remote Sens., 52, 3159-3174 (2014).
16. J. Sun, A. Angal, X. Xiong, H. Chen, X. Geng, A. Wu, T. Choi, and M. Chu, "MODIS RSB calibration improvements in Collection 6", Proc. SPIE 8528, 85280N (2012).
17. J. Sun, X. Xiong, and W. Barnes, "MODIS Solar Diffuser Stability Monitor Sun View Modeling", IEEE Trans. Geosci. Remote Sens., 43, 1845-1854 (2005).
18. J. C. Cardema, K. Rausch, N. Lei, D. I. Moyer, F. DeLuccia, Operational calibration of VIIRS reflective solar band sensor data records. Proc. SPIE 8510, 851019 (2012).
19. N. Lei, Z. Wang, J. Fulbright, S. Lee, J. McIntire, K. Chiang, and X. Xiong, "Initial on-orbit radiometric calibration of the Suomi NPP VIIRS reflective solar bands," Proc. SPIE, 8510, 851018 (2012).